Experimental and Computational Multiphase Flow
Vol. 6, No. 1, 2024, 67–83
https://doi.org/10.1007/s42757-023-0159-9

Analysis of two-phase flow in the porous medium through a rectangular curved duct

Khalilur Rahman[1,2] (✉), Salma Parvin[2], Abdul Hakim Khan[2]

1. Department of Mathematics, Bangladesh Civil Service, Ministry of Education, Dhaka 1000, Bangladesh
2. Department of Mathematics, Bangladesh University of Engineering & Technology, Dhaka 1000, Bangladesh

Abstract

The current work is primarily concerned with the analysis of an unsteady incompressible laminar two-phase flow in a porous medium through a rectangular curved duct. The Navier–Stokes equations and the level set equation with boundary conditions represent the corresponding governing equations. Fluid flow through curved rectangular ducts is influenced by the centrifugal action arising from duct curvature and has a unique behavior different from fluid flow through straight ducts. Centrifugal force-induced secondary flow vortices produce spiraling fluid motion within curved ducts. This paper shows the vector plot of the field flow, velocity contours, and fluid volume fractions graphically. The effect of curvature, Dean number, aspect ratio, porosity, and particle concentration on each fluid domain is also displayed. A comparison of the two-phase flow between different fluids is also shown. The results reveal that the unstable behavior of the flow is reduced with increased values of curvature, Dean number, and high viscosity flow.

Keywords

rectangular curved duct
Dean number
two-phase flow
finite element method
porous medium

Article History

Received: 9 August 2022
Revised: 29 December 2022
Accepted: 29 January 2023

Research Article

1 Introduction

In fluid mechanics, the flow across curved channels is a topic of fundamental research interest. The most prevalent flow in natural rivers is channel flow. Such channels are commonly constructed in nations that generate oil. Engineering applications include heat exchangers, turbomachinery blade passageways, aircraft intake diffusers, and biological transport phenomena. Eustice (1910, 1911) made the initial discovery of the existence of this secondary flow pattern by injecting dyes into a curved pipe flow stream. Dean (1927, 1928) conducted an analysis and found that the Dean number, a single parameter, could adequately describe the flow of curved pipes. Laminar secondary flows in curved rectangular ducts were investigated by Thangam and Hur (1990). In a curved duct with an elliptic flow, Dong and Ebadian (1992) numerically investigated the effects of buoyancy on fully developed laminar flow. Hoque and Alam (2013) investigated how the curvature of a curved pipe and the Dean number affect fluid flow through the pipe. In a curved channel with vortex features, laminar forced convection was experimentally studied by Avramenko et al. (2004). The results of the experiments revealed that both linear and nonlinear components grew with the Dean number. In curved channels, Stokes flow was explored by Khuri (2006). In a constant-area curved duct, tests on flow study were conducted by Biswas et al. (2012). Mathematical analysis of the peristaltic flow of a two-phase nanofluid in a curved conduit was conducted by Nadeem and Shahzadi (2015). In a corrugated, curved channel, fluid motion was examined by Okechi and Asghar (2019). Khan and Hye (2007) investigated the flow's dominant singularity in a straight, non-aligned rotating pipe. Khan (2006) examined the singularity behavior of flow in a curved pipe. The prediction of non-isothermal flows via a rotating, curving duct with a square cross-section was examined numerically by Mondal et al. (2007). Norouzi and Biglari (2013) examined the Dean flow in a curved duct with a rectangular cross-section.

Multiphase flow has great importance in experimental research and has broad applications. Two-phase flow is

✉ 0418094001@math.buet.ac.bd

Nomenclature

c_p	Specific heat at constant pressure	u, v, w	Velocity in X, Y, Z axis, respectively
d	Width of the curved duct (m)	x, y, z	Cartesian coordinates
De	Dean number	γ	Re-initialization parameter
g	Gravitational acceleration	ε	Thickness of interface
h	Height of the curved duct (m)	μ	Dynamic viscosity of the fluid
K	Porosity	ν	Kinematic viscosity of the fluid
L	Radius of curvature (m)	ρ	Density of the fluid
P	Pressure	φ	Level set function
Re	Reynolds number	ϕ	Particle concentration
t	Dimensional time		

essential in hydraulic conveying, liquid mixing, liquid separations, liquid extraction, steam generators, jet engines, condensers, and distillation processes in the pipeline. Xu et al. (1999) experimentally studied gas–liquid two-phase flow regimes in rectangular channels with mini/micro gaps. Crandall et al. (2009) compared experimental results and the numerical result of two-phase flows in a porous micro-model. Garg et al. (2014) and Picardo et al. (2015) investigated the fully developed flow field of two vertically stratified fluids in a curved channel of a rectangular cross-section. A numerical investigation of two-phase flows through the enhanced micro-channel was conducted by Chandra et al. (2016). Al-Jibory et al. (2018) discussed an experimental and numerical study for two-phase flow (water and air) in rectangular ducts with compound tabulators. Okechi and Asghar (2021) studied two-phase flow in a grooved, curved channel.

The level set method (LSM) is a useful tool in physics, engineering, materials science, computer graphics, and beyond. The LSM has been most commonly used for phase transformations and multiphase flow. Osher and Sethian (1988) introduced LSM, which creates new algorithms for following fronts propagating with curvature-dependent speed derived from the Hamilton–Jacobi equation. Furthermore, this level set approach has been applied to incompressible two-phase flow since the article of Sussman et al. (1994). Olsson and Kreiss (2005, 2007) discussed the conservative LSM two-phase flow. Datta et al. (2011) studied analytical and LSM-based studies for two-phase stratified flow in a plane channel and a square duct. LSM for computational multi-fluid dynamics was studied by Sharma (2015).

The flow through porous media scheme piques the interest of engineers and scientists. There is also the eagerness of politicians and economists who see the importance of groundwater flows and a variety of tertiary oil recovery processes. Bear (1972) summarized the application of flow through porous media in his book. Greenkorn (1981) discussed the pseudo transport coefficients permeability, capillary pressure, and dispersion as well as the fundamentals of steady flow through porous media. Dwivedi et al. (2018) studied magnetohydrodynamics (MHD) flow through a vertical channel with a porous medium. Devakar et al. (2017) numerically studied the fully developed flow of non-Newtonian fluids in a straight, uniform square duct through a porous medium. Hellström (2007) studied the parallel computing of fluid flow through porous media. Roy et al. (2020) presented a theoretical study for immiscible two-phase flow in homogeneous porous media. Chowdhury et al. (2016) analyzed natural convective heat and mass transfer in a porous triangular enclosure filled with nanofluid in the presence of heat generation.

The numerical analysis of two-phase flow in the porous medium through the rectangular curved duct has not yet been found in the open literature. In order to solve the Navier–Stokes equations with boundary conditions in the aforementioned issue, the finite element method is used in this paper. For a clearer understanding of the impacts of curvature, the Dean number, aspect ratios, porosity, and particle concentration on each domain, the vector plot of the field flow, the velocity contour, and the volume fraction of fluid on the domain are shown for various time points. Additionally, the findings for various fluids in the outer domain are compared.

2 Mathematical model

An unsteady incompressible viscous laminar three-dimensional (3D) two-phase flow is considered here. The flow passes in the porous medium through a curved duct with a rectangular cross-section. The height and the width of the cross-section are h (m) and d (m), respectively. O is the center of the curvature and L (m) is the radius of curvature of the duct, as shown in Fig. 1. The analysis uses a mixture of water and engine oil as the immiscible working fluid, which is sustained together into the curved duct path. In the curved channel inlet, engine oil enters the outer

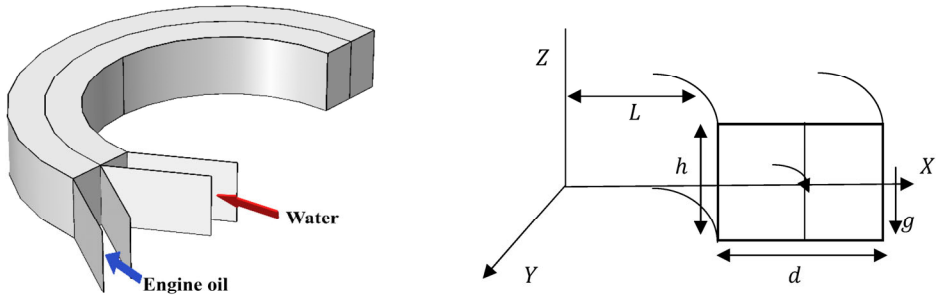

(a) (b)

Fig. 1 (a) Cross sectional view and (b) coordinate system.

domain, and water enters the inner domain with different velocities. Although the inlet velocity is different, the Reynolds number remains the same for the fluid in both domains. All physical properties of fluids are assumed constant.

The mathematical model can be expressed by the governing equations according to Kucuk (2010) and Gyves (1997):

$$\text{Continuity equation: } \frac{\partial u}{\partial x}+\frac{\partial v}{\partial y}+\frac{u}{x+L}=0 \tag{1}$$

Momentum equations:

$$\frac{\partial u}{\partial t}+u\frac{\partial u}{\partial x}+v\frac{\partial u}{\partial y}-\frac{w^2}{x+L} =-\frac{1}{\rho}\frac{\partial P}{\partial x}+\nu\left[\frac{\partial^2 u}{\partial x^2}+\frac{\partial^2 u}{\partial y^2}+\frac{1}{x+L}\frac{\partial u}{\partial x}-\frac{u}{(x+L)^2}\right]-\frac{\mu u}{K} \tag{2}$$

$$\frac{\partial v}{\partial t}+u\frac{\partial v}{\partial x}+v\frac{\partial v}{\partial y}=-\frac{1}{\rho}\frac{\partial P}{\partial y}+\nu\left(\frac{\partial^2 v}{\partial x^2}+\frac{1}{x+L}\frac{\partial v}{\partial x}+\frac{\partial^2 v}{\partial y^2}\right)-\frac{\mu v}{K} \tag{3}$$

$$\frac{\partial w}{\partial t}+u\frac{\partial w}{\partial x}+v\frac{\partial w}{\partial y}+\frac{uw}{x+L}=-\frac{1}{\rho}\frac{1}{(x+L)}\frac{\partial P}{\partial z}+ \nu\left[\frac{\partial^2 w}{\partial x^2}+\frac{\partial^2 w}{\partial y^2}+\frac{1}{x+L}\frac{\partial w}{\partial z}-\frac{w}{(x+L)^2}\right]-g \tag{4}$$

where u, v, and w are velocity components in the x, y, and z directions, respectively; ρ is the density, ν is the kinematic viscosity, L is the radius of curvature, and K is the porosity of the medium. The model neglects all terms of the order $\frac{1}{L}$ and $\frac{1}{L^2}$, except the centrifugal force term as in Gyves et al. (1999).

The boundary conditions at the channel, the core walls, and the inlet and outlet are

$$(u,v,w)=0 \text{ at } r=L=\sqrt{x^2+y^2},\ r=L+d, \text{ top and bottom wall} \tag{5}$$

$$\begin{aligned}&\text{At the inlet-1} && u=u_1\hat{n}\\ &\text{At the inlet-2} && u=u_2\hat{n}\\ &\text{At the outlet} && P=P_0\end{aligned} \tag{6}$$

The Dean number De is typically denoted by

$$De=Re\left(\frac{d}{L}\right)^{1/2} \tag{7}$$

where Re is the Reynolds number, d is a typical length scale associated with the channel cross-section, and L is the radius of curvature of the path of the duct. Re is defined by

$$Re=\frac{\rho d u}{\mu} \tag{8}$$

where ρ and μ are density and dynamical viscosity of the fluid, respectively. Since the governing equations are non-dimensional and ρ, d, and μ are considered constant, De as well as Re depend on the value of u.

Porosity can be written as

$$K=\frac{V-V_s}{V}=\frac{V_p}{V} \tag{9}$$

where V is the bulk rock volume that is not occupied by solid matter, V_s is the volume of solid, and $V_p=V-V_s$ is the pore volume.

The level set function φ can be represented by Eq. (10) from Olsson and Kreiss (2007).

$$\frac{\partial \varphi}{\partial t}+\boldsymbol{u}\cdot\nabla\varphi=\gamma\nabla\cdot\left[\varepsilon\nabla\varphi-\varphi(1-\varphi)\frac{\nabla\varphi}{|\nabla\varphi|}\right] \tag{10}$$

where $\boldsymbol{u}$ is the fluid velocity. The ε parameter determines the thickness of the layer of the interface. The γ parameter determines the amount of reinitialization, and φ is the level set function that varies from 0 to 1. For engine oil $\varphi=0$, and for water $\varphi=1$.

The level set function φ is defined by

$$\varphi(x) = \begin{cases} 0, & x \in \text{phase 1} \\ 1, & x \in \text{phase 2} \end{cases} \tag{11}$$

For calculating surface tension, the interface normal and curvature are obtained according to the sign function

$$\overline{n} = \left.\frac{\nabla\varphi}{|\nabla\varphi|}\right|_{\varphi=0} \quad \text{and} \quad k = \nabla\cdot\left.\frac{\nabla\varphi}{|\nabla\varphi|}\right|_{\varphi=0} \tag{12}$$

The level set function is used to determine the density and dynamic viscosity globally by

$$\rho = \rho_{\text{Eo}} + (\rho_{\text{w}} - \rho_{\text{Eo}})\varphi \tag{13}$$

$$\mu = \mu_{\text{Eo}} + (\mu_{\text{w}} - \mu_{\text{Eo}})\varphi \tag{14}$$

where ρ_{Eo} and ρ_{w} are the density of engine oil and water, respectively; μ_{Eo} and μ_{w} are the dynamic viscosity of engine oil and water, respectively.

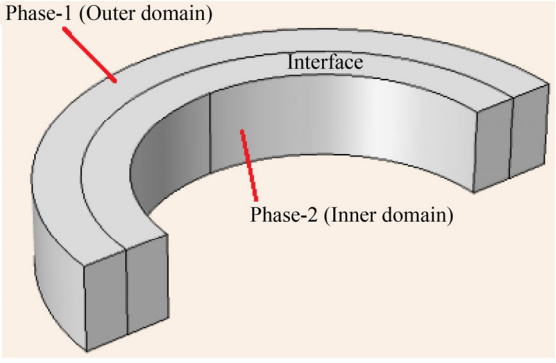

Fig. 2 Phase distribution.

3 Numerical solution

To build a simulation, the entire structure must be divided into small elements called mesh, and calculations are done for each individual element. Combining the individual results gives the final result of the structure. Among the elements that are taken, we know the values at certain points but not on each point. These "fixed points" are called nodal points and are often located at element boundaries. The finite element method formulation of a boundary value problem finally results in a system of algebraic equations, and the system of algebraic equations will be solved by matrix formula. For a system with a large number of linear algebraic equations, it is impossible to solve manually. Usually software is used to solve such a problem. COMSOL Multiphysics is a finite element analysis solver and simulation program for a variety of physics and engineering applications, particularly for coupled phenomena and multiphysics. The program enables coupled systems of partial differential equations with standard physics-based user interfaces.

The finite element meshing of the computational domain is displayed in Fig. 3. A grid refinement test was performed until the results showed insignificant change for further refined mesh size.

From Table 1 it was observed that results for average velocity magnitude have no significant changes up to three decimal places for normal and fine mesh size. Therefore, normal mesh size was chosen to find the grid independent solution and to save computational time.

Earlier, the solution of the vector plot of flow parameters in a square curved duct was established by Norouzi and Biglari (2013). They studied single-phase flow and used the perturbation method to solve governing equations with the boundary condition, and their result is shown in Fig. 4(a). In the present study, their result has been reproduced by using the finite element method, which is shown in Fig. 4(b). It was observed that both results are almost the same. Therefore, the present numerical method is in good agreement with the work presented by Norouzi and Biglari (2013).

4 Results and discussion

In a curved duct, the centrifugal action manifests two key effects. It generates a positive radial pressure field directed towards the outer duct wall. The centrifugal force drives the fluid radially from the inner to the outer duct wall within the positive pressure field, setting up lateral fluid circulation called secondary flow. The secondary fluid motion becomes vigorous and the radial pressure field intensifies when axial flow increases. Assisted by fluid viscosity, this positive pressure field adversely affects the secondary fluid flow

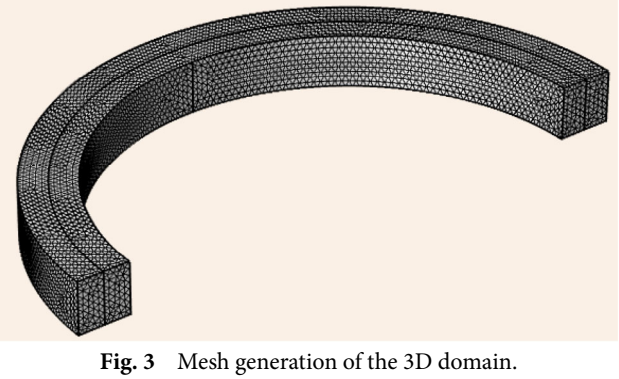

Fig. 3 Mesh generation of the 3D domain.

Table 1 Element size comparison

Mesh size	Extremely coarse	Extra coarse	Coarse	Coarser	Normal	Fine
Number of elements	2256	6448	18,196	61,314	131,956	389,530
Average velocity	0.049449	0.079742	0.108142	0.132178	0.146304	0.146781

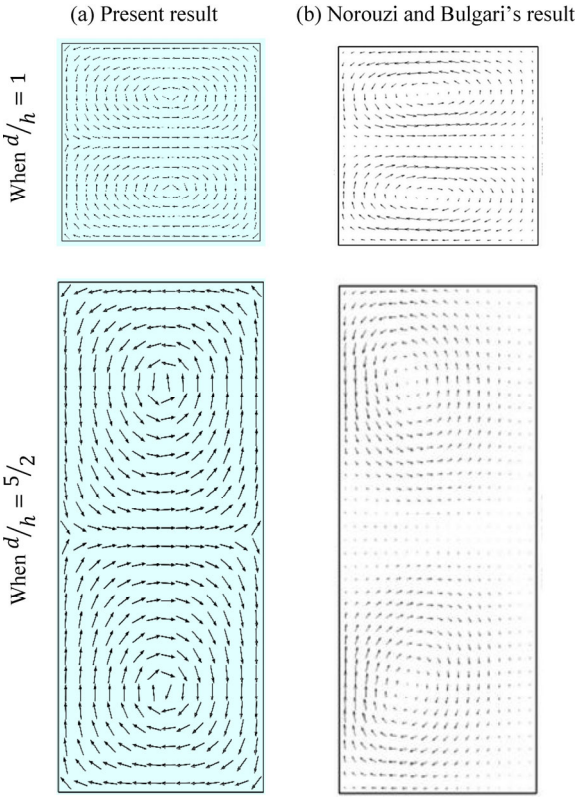

Fig. 4 Comparison of numerical solution of vector plot of flow with $Re = 50$ and $\delta = 0.1$.

moving towards the outer duct wall to slow it down. Consequently, near the outer duct wall, a stagnant flow region is formed.

The solution for the unsteady incompressible laminar two-phase fluid flow through a 3D rectangular curved channel has been displayed here. The results in terms of axial flow velocity, velocity contour, and vector plot of flow field have been discussed for the various radius of curvature ($20\text{ m} \le L \le 100\text{ m}$), Dean number ($45 \le De \le 1800$), aspect ratio (1:1 to 1:6), particle concentration of outer domain ($0.0 \le \phi \le 1$), and several time steps (0–300 s). Also, five different fluids (engine oil, kerosene, ethylene glycol, heptane, glycerol, and ethanol) have been tested in the outer domain. All the figures are taken at the cut plane of $Y - Z$ plane at $x = 0$.

Figure 5(a) shows volume fraction visualization for different moments. At time $t = 0$ s the multiphase fluid located in different areas. Water enters the inner domain (red), engine oil enters the outer domain (blue), and yellow denotes the domain interface. The multiphase flow will mix with time.

Low-viscosity fluid will be in the upper portion, while high-viscosity fluid will be in the lower portion. The interface will also appear periodic at $t = 60$ and 120 s, and the mixed fluid will reach steady-state at $t \ge 300$ s.

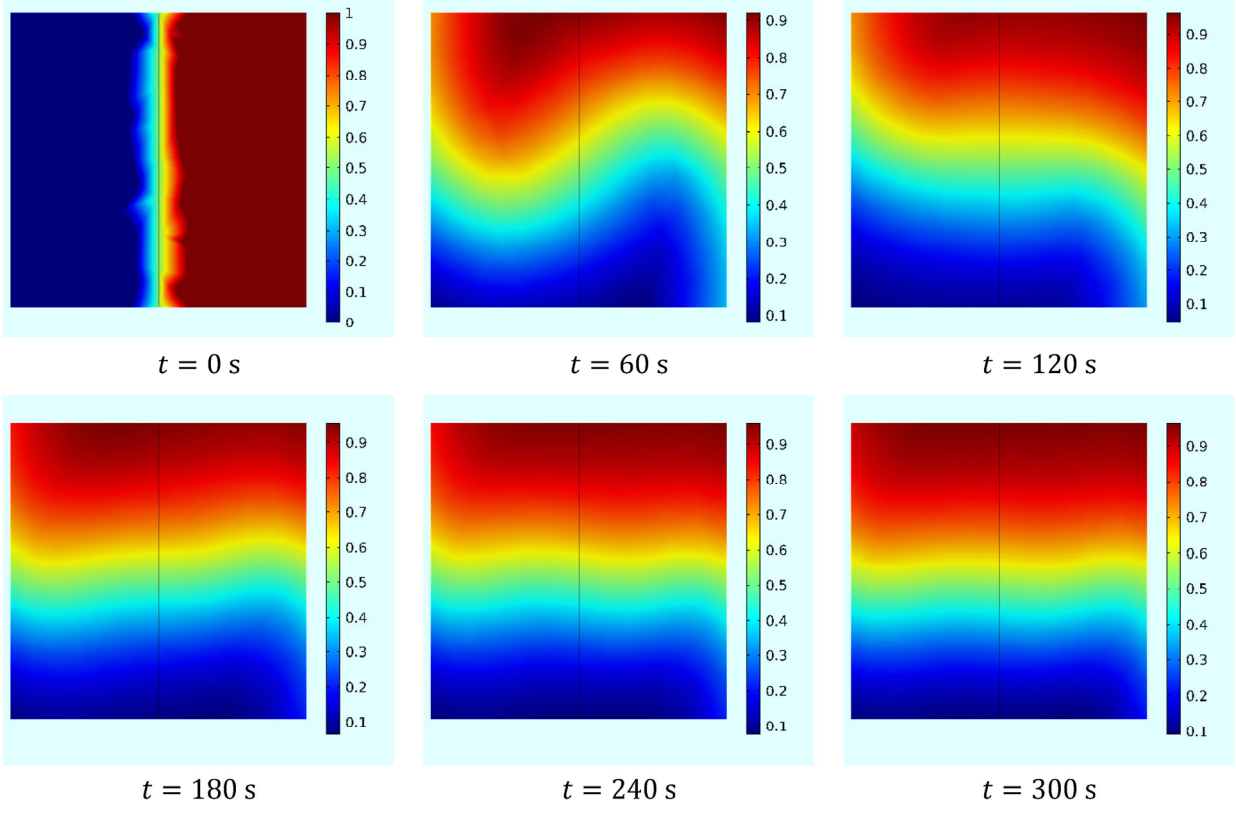

Fig. 5(a) Volume fraction visualization at different time with $De = 180$, $L = 40$ m, and $\phi = 0.0$ at outer domain for aspect ratio 1:1.

Figure 5(b) shows the velocity contour of flow. When $t = 60$ s, at the upper part of the duct cross-section, four additional contours could be seen inside the principal vortex. It suggests that the Dean's flow does have a rotating form. When $t = 120$ and 240 s, the axial flow is displaced adjacent to the inner and outer walls of the duct, and there are 6–8 contours. The chaotic Dean's flow is represented by it as well. At $t = 150, 180$, and 300 s, axial flow is spread over both domains, and there are 10–12 contours. Also, this demonstrates exactly how chaotic the Dean's flow is.

A vector plot of the flow field is shown in Fig. 5(c). At $t = 60$ s there is a single vortex solution at the center of the duct. Two solution vortices for secondary flow are present

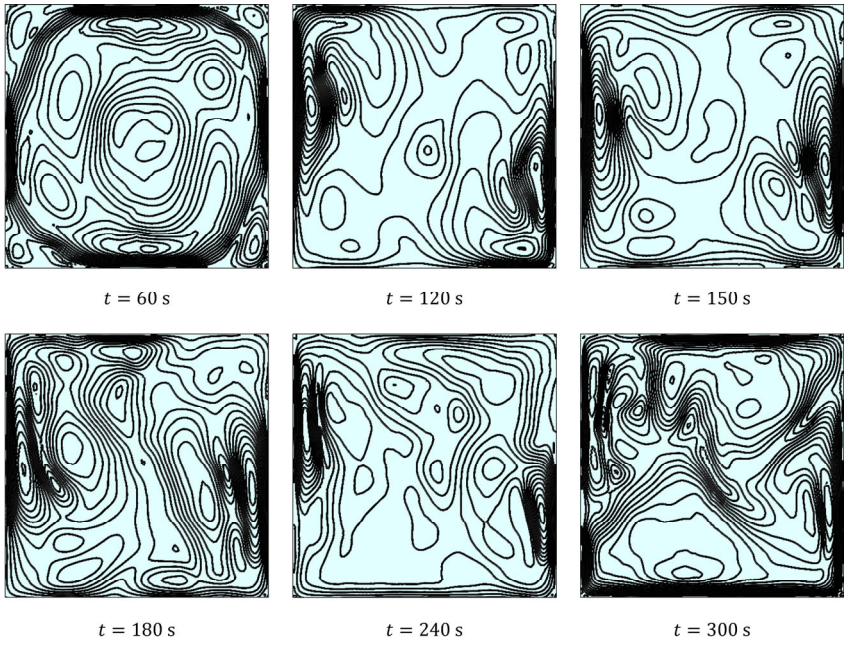

Fig. 5(b) Velocity contour at different time with $De = 180$, $L = 40$ m, and $\phi = 0.0$ at outer domain for aspect ratio 1:1.

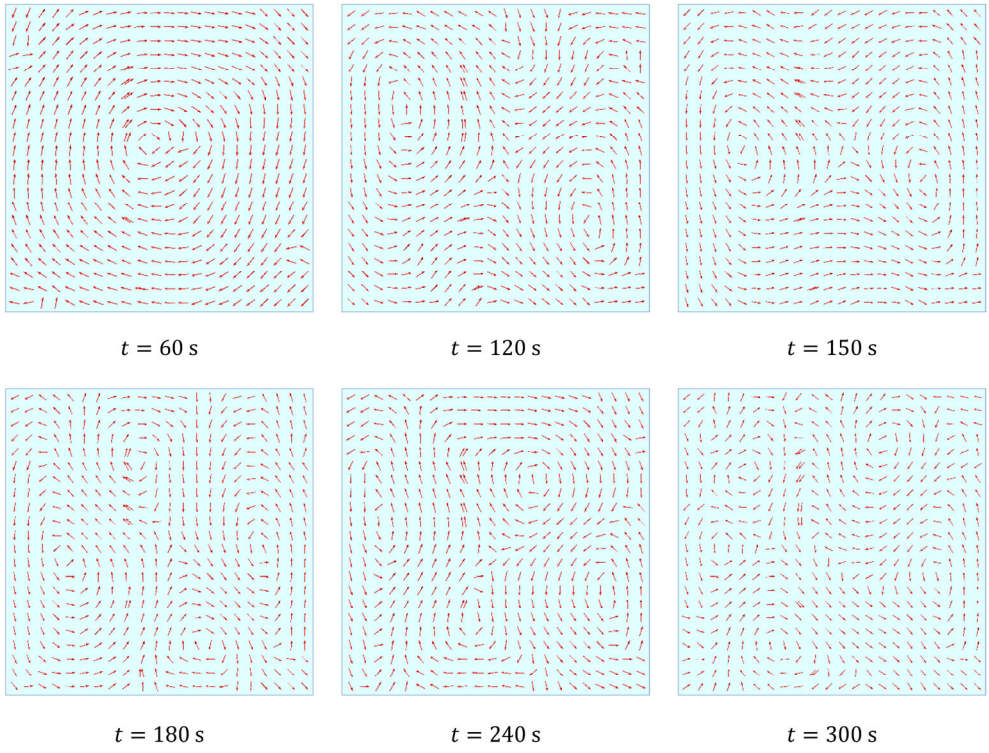

Fig. 5(c) Vector plot of flow field at different time with $De = 180$, $L = 40$ m, and $\phi = 0.0$ at outer domain for aspect ratio 1:1.

at the same time, along with just a few line segments along the wall. At $t = 180$ and 240 s, for secondary flow there are four distinct vortex solutions, and each pair of vortex is pointing in reversed directions. Also at $t \geq 300$ s, there are six symmetric vortexes, with each pair pointing in opposite directions as well.

Figure 5(d) shows that when $t = 0$ s the axial flow velocity is in a straight line since the flow velocity is zero. When $t = 60$ and 240 s, the low-viscosity fluid flows faster than the high-viscosity fluid, and the axial flow velocity of mixed fluid is hyperbolic and produces multiple orbits. Also at $t = 120$ s, high-viscosity fluid flows at a faster speed than low-viscosity fluid in a spiral pattern in the axial direction. But when $t = 240$ s, low-viscosity fluid moves faster in the axial direction in a spiral manner. Finally, when $t = 300$ s, the axial velocity of the mixed fluid is hyperbolic and only generates two orbits, and low-viscosity fluid flows at a faster rate than high-viscosity fluid.

The impact of the radius of curvature on the velocity contour is seen in Fig. 6(a). When L = 20 m, the axial flow is relocated closer to the duct's outer wall, and it is apparent that there are 14 contours. It manifests chaotic Dean's flow. But when L = 40 and 60 m, there are six contours, which means that the axial flow is shifted closer to the duct's outer wall, and also illustrates the chaotic nature of the Dean's flow. When L = 80 m, at the top of the duct cross-section, where contours tend to gather in the center, there are four additional contours inside the principal contour than when L = 100 m. It implies a stable condition for the Dean's flow. Finally, when L = 1000 m, only one principal contour can be found in the outer domain, and it behaves as a straight closed channel or duct.

The vector plot of the flow field is highlighted by the curvature radius's impact in Fig. 6(b). When L = 20 and 40 m, for symmetric secondary flow, there are six vortex solutions. Each pair of vortices is moving in opposition to one another. For secondary flow, there are two symmetric vortex solutions for L = 80 m, and three asymmetric vortex solutions for L = 60 m. Each pair of vortices is in opposite direction. The single vortex solution exists at L = 100 m. When L > 100 m, there is only one vortex that oscillates on the centerline, suggesting that the flow behavior may approach a parallel channel. There is no vortex solution at L = 1000 m.

Figure 6(c) illustrates how the curvature radius changes the axial flow velocity. When L = 20 m, the mixed fluid's axial flow velocity seems to have a hyperbolic shape and generates multiple orbits, with the high-viscosity fluid moving at a faster

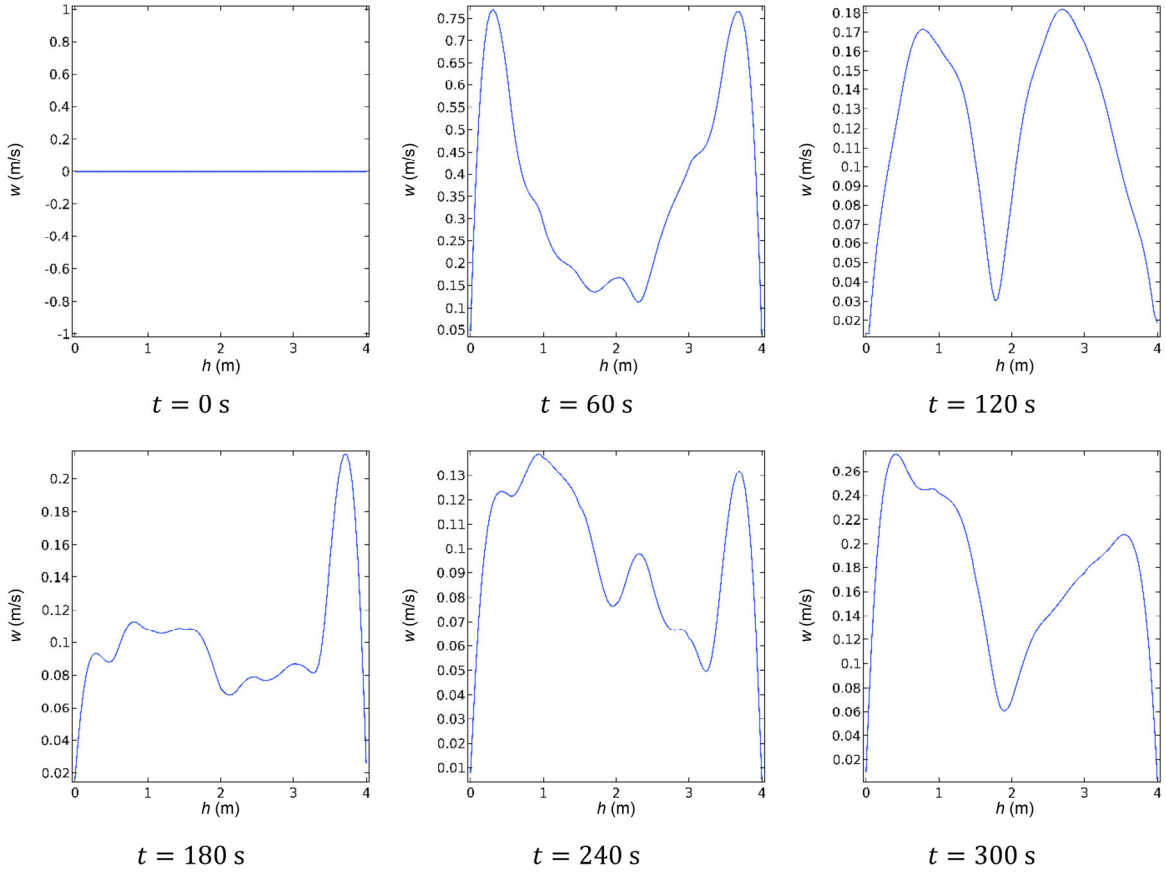

Fig. 5(d) Axial flow velocity at different time with De = 180, L = 40 m, and ϕ = 0.0 at outer domain for aspect ratio 1:1.

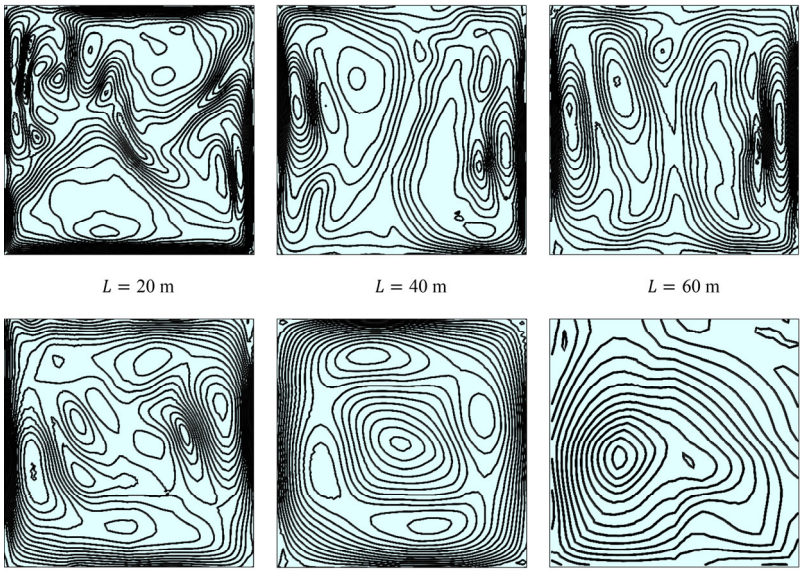

Fig. 6(a) Effect of radius of curvature on velocity contour with $De = 180$, $t = 300$ s, and $\phi = 0.0$ at outer domain for aspect ratio 1:1.

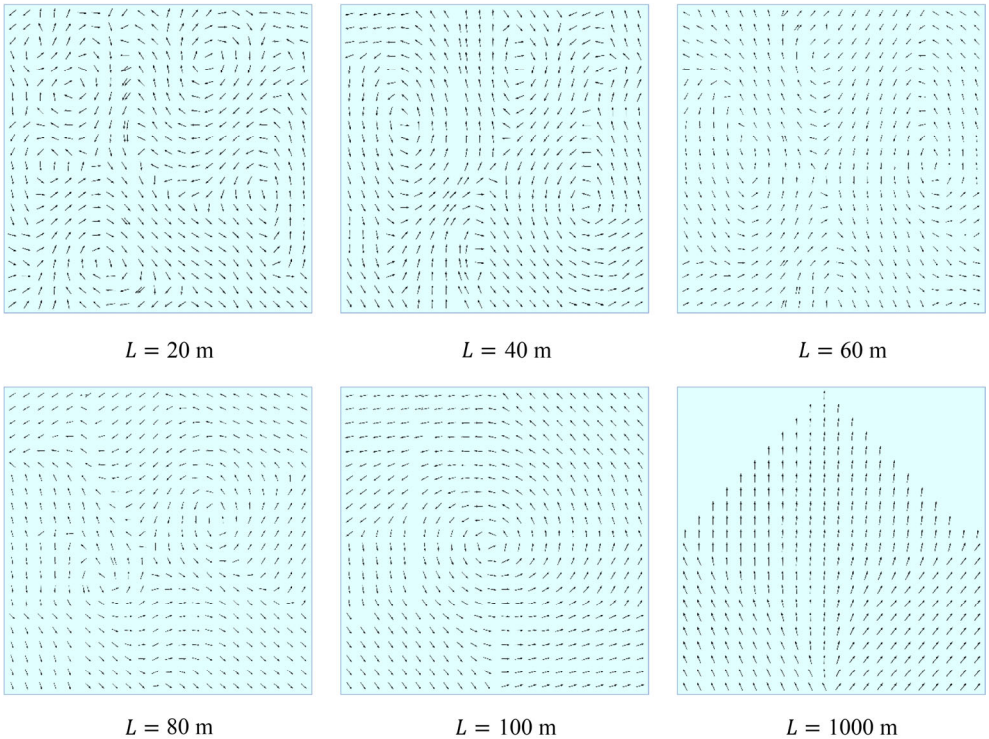

Fig. 6(b) Effect of radius of curvature on vector plot of flow field with $De = 180$, $t = 300$ s, and $\phi = 0.0$ at outer domain for aspect ratio 1:1.

rate than the low-viscosity fluid. For $L = 40$ m, the axial flow velocity of the mixed fluid exhibits two orbits and a parabolic shape, with the low-viscosity liquid faster than the high-viscosity fluid. Another finding is that the axial flow velocity of the mixed fluid has a meandering shape at $L = 60$ m, and is quite high along the fluid-to-fluid interface. When $L = 80$ m, the mixed fluid's axial velocity is hyperbolic, producing multiple orbits, and the velocity of the low-viscosity fluid is higher than that of the high-viscosity fluid. But when $L = 100$ m, the axial flow velocity is hyperbolic with two orbits, and the low-viscosity fluid flows at a faster rate than the high-viscosity fluid. At $L = 1000$ m, only one orbit has axial flow velocity.

Effects of the Dean number on velocity contour are shown in Fig. 7(a). When $De = 45$ and 180 there are 8–10 contours, and the axial flow is shifted near the outer wall

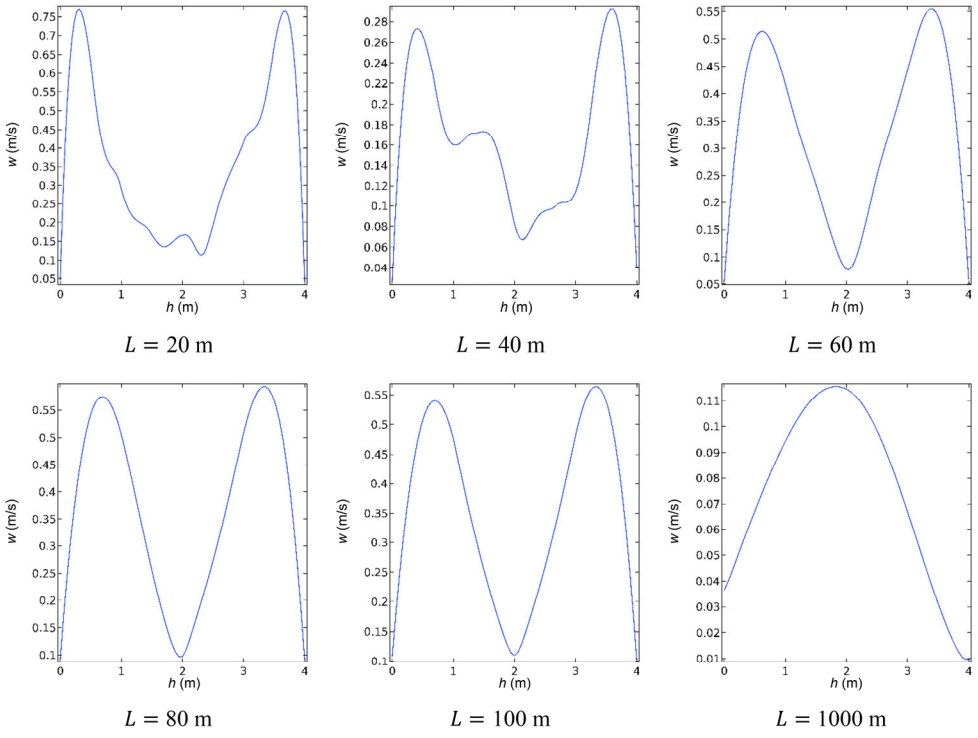

Fig. 6(c) Effect of radius of curvature on axial flow velocity with $De = 180$, $t = 300$ s, and $\phi = 0.0$ at outer domain for aspect ratio 1:1.

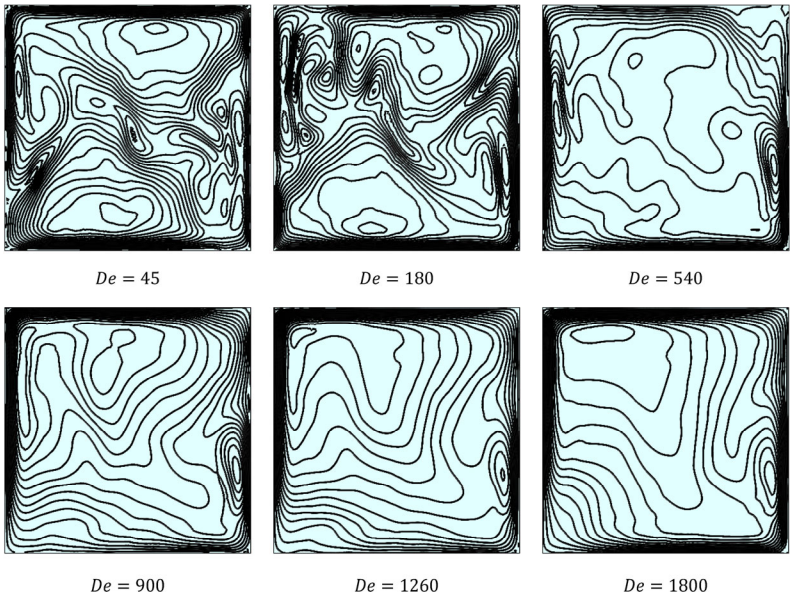

Fig. 7(a) Effect of Dean number on velocity contour with $L = 40$ m, $t = 300$ s, and $\phi = 0.0$ at outer domain for aspect ratio 1:1.

of the duct. It shows that Dean's flow is strongly chaotic. When $De = 540$ and 900 there are 2–4 contours, and the axial flow is shifted near the outer wall of the duct. It also shows that Dean's flow is chaotic. But when $De = 1260$ and 1800 there are only two contours, and the axial flow is shifted near the inner wall of the duct. That means the Dean's flow is becoming steady state.

From Fig. 7(b), when $De = 45$, 180, 540, and 900, for secondary flow, there are six symmetric solutions containing opposing directional vortices. Similar to this, there are two symmetric solution vortices with opposing directions when $De = 1260$.

For $De = 1800$, the inner domain consists of one vortex solution location and a few parallel lines that travel along the wall.

Figure 7(c) shows the impact of the Dean's number on axial flow velocity. With $De = 45$, the mixed fluid's axial flow velocity exhibits hyperbolic axial flow, resulting in multiple

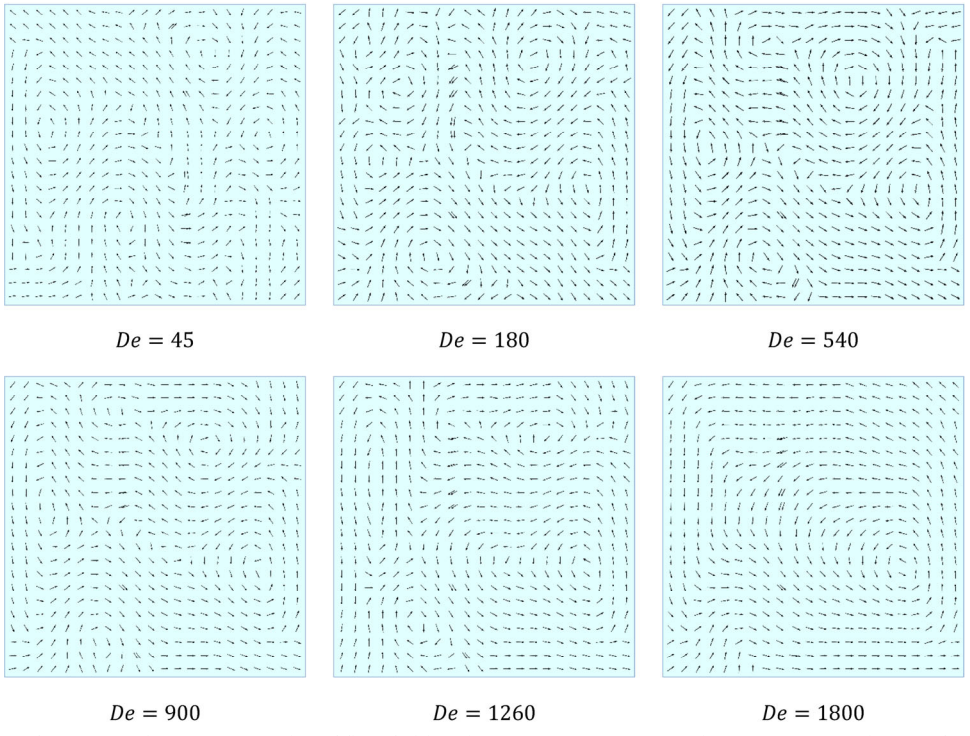

Fig. 7(b) Effect of Dean number on vector plot of flow field with L = 40 m, t = 300 s, and ϕ = 0.0 at outer domain for aspect ratio 1:1.

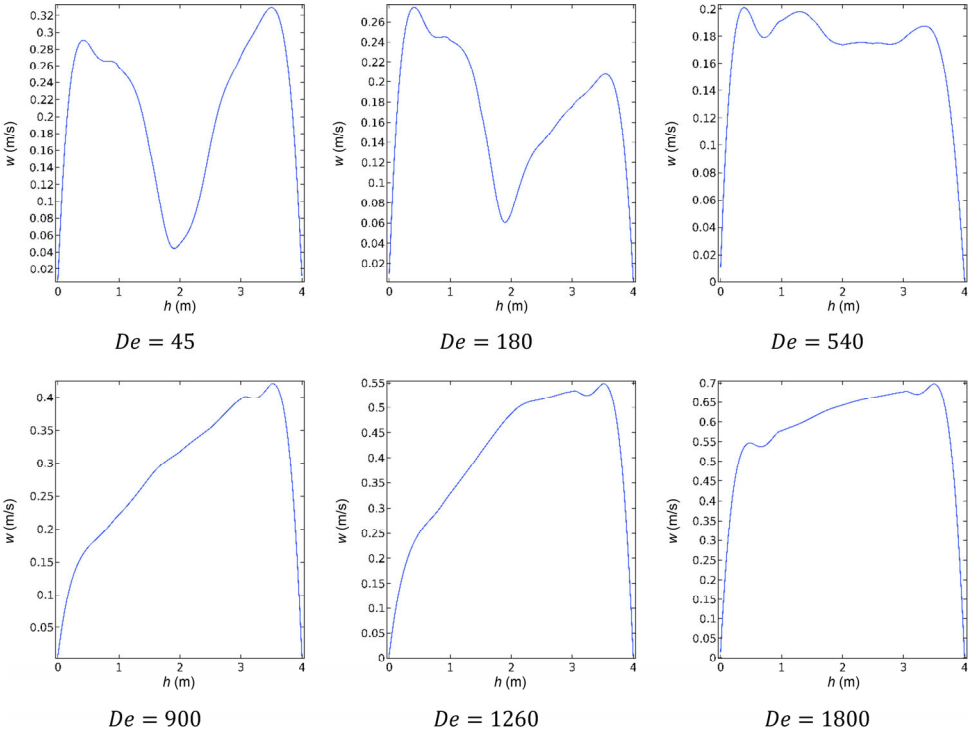

Fig. 7(c) Effect of Dean number on axial flow velocity with L = 40 m, t = 300 s, and ϕ = 0.0 at outer domain for aspect ratio 1:1.

orbits. Additionally, it demonstrates that for De = 45, low-viscosity fluid has a higher velocity than high-viscosity fluid, while for De = 180, high-viscosity fluid has a higher velocity than low-viscosity fluid. The axial flow velocity has an erratic pattern when De = 450, with high-viscosity fluid moving more swiftly than low-viscosity fluid. Again, when De = 900, 1260, and 1800, axial flow velocity is in the shape of a curving line, and the velocity of low-viscosity fluid is higher than that of high-viscosity fluid.

Figure 8(a) depicts the impact of particle concentration

on the velocity contour at the first domain (outer domain). When $\phi = 0.2$, the outer domain includes 20% water and the inner domain includes 80% engine oil.

As can be seen in Fig. 8(a), when $\phi = 0.0, 0.2, 0.8,$ and 1.0, it demonstrates the presence of 10–12 contours and the axial flow's displacement is towards the duct channel and inner wall channel's centre. So Dean's flow is chaotic. But when $\phi = 0.4$ and 0.6, it demonstrates the presence of 8–10 contours and the axial flow's shift is towards the duct channel's center. The Dean flow is similarly chaotic.

Figure 8(b) illustrates how particle concentration affects the vector plot of the flow field in the outer domain. There are six symmetric vortex solutions for secondary flow at $\phi = 0.0, 0.2, 0.4, 0.6, 0.8,$ and 1.0, and each pair of vortex

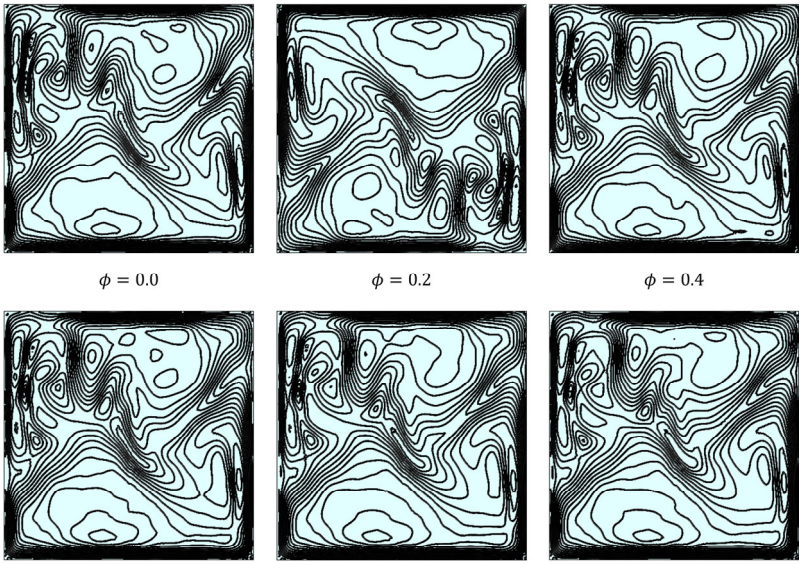

Fig. 8(a) Effect of particle concentration on velocity contour with De = 180, t = 300 s, and L = 40 m at outer domain for aspect ratio 1:1.

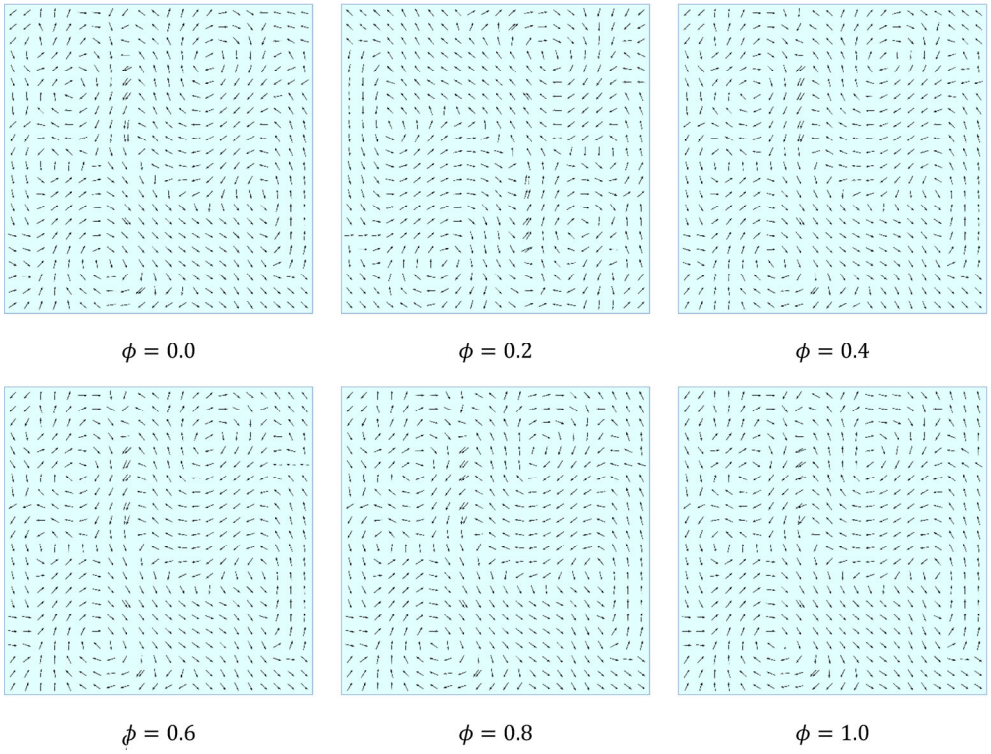

Fig. 8(b) Effect of particle concentration on vector plot of flow field with De = 180, t = 300 s, and L = 40 m at outer domain for aspect ratio 1:1.

pairs is pointed in reverse directions, as can be seen in Fig. 8(b).

Axial flow velocity is depicted to show the impact of particle concentration in Fig. 8(c). The axial flow velocity has a hyperbolic curve and produces numerous orbits when $\phi = 0.0, 0.2, 0.4, 0.6, 0.8$, and 1.0. It has been noted that high-viscosity fluid has a higher axial velocity than low-viscosity fluid.

In Fig. 9, the axial flow velocity, velocity contour, and vector plot of the flow field on the cut plane are compared for several fluids on two domains. Engine oil, kerosene, ethylene glycol, heptane, ethanol, and glycerol were used in the outer domain, while water was used in the inner domain, comparing six different fluids.

By comparing two-phase flow between various fluids, it is found that ethanol has a very high viscosity while kerosene has a very low viscosity (Table 2). Eight to ten contours are created by the mixed fluid flow of water with heptane, kerosene, glycerol, and engine oil, as can be seen in Fig. 9(a), and the axial flow is displaced adjacent to the inner and outer duct walls. The Dean's flow is a mess because of this. Once more, water–ethanol produces 4–6 contours, indicating that the axial flow is shifted near the duct's outer and inner walls. Dean's flow is therefore similarly chaotic. Last but not least, water–ethylene glycol only generates two contours and displays how axial flow is shifted toward the top and bottom of the duct. The Dean's flow is becoming steady.

According to Fig. 9(b), there are six symmetric vortex solutions for fluid mixtures of water and heptane, kerosene, glycerol, ethylene glycol, and engine oil, and each of the vortex pairs is pointing in the reverse way. Two symmetric and two asymmetric vortex formations can be found in reverse for water–ethanol. It also demonstrates the reversed rotation of symmetric vortices.

Figure 9(c) demonstrates the hierarchical configuration with multiple orbits of the mixed fluid flow for water–heptane, water–kerosene, water–ethylene glycol, water–glycerol, and water–engine oil. Nevertheless, water–ethanol mixtures have a curved axial flow velocity. It also demonstrates that for these six types of mixtures, the velocity of high-viscosity fluid is greater than that of low-viscosity fluid. The velocity of the low-viscosity fluid is higher in the reverse direction of the mixed flow of water, ethylene, and glycol, which likewise has a hyper pattern with just two orbits. In the reverse direction, the mixed flow of water and ethylene glycol has a hyperbolic

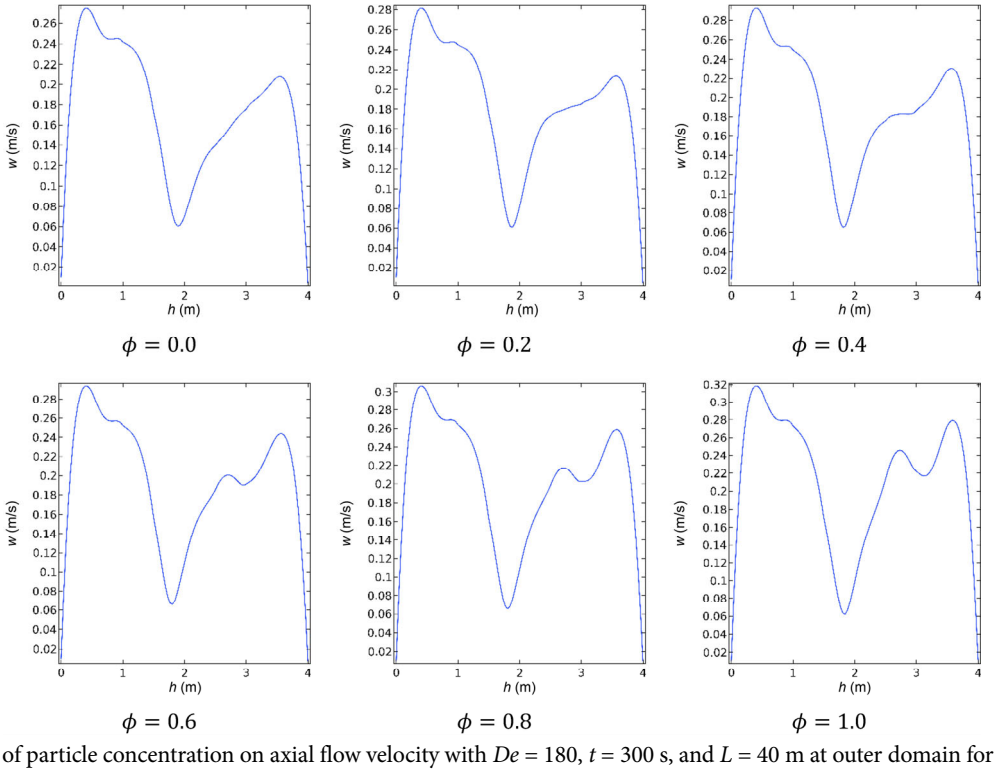

Fig. 8(c) Effect of particle concentration on axial flow velocity with $De = 180$, $t = 300$ s, and $L = 40$ m at outer domain for aspect ratio 1:1.

Table 2 Element size comparison

Mesh size	Extremely coarse	Extra coarse	Coarse	Coarser	Normal	Fine
Number of elements	2256	6448	18,196	61,314	131,956	389,530
Average velocity	0.049449	0.079742	0.108142	0.132178	0.146304	0.146781

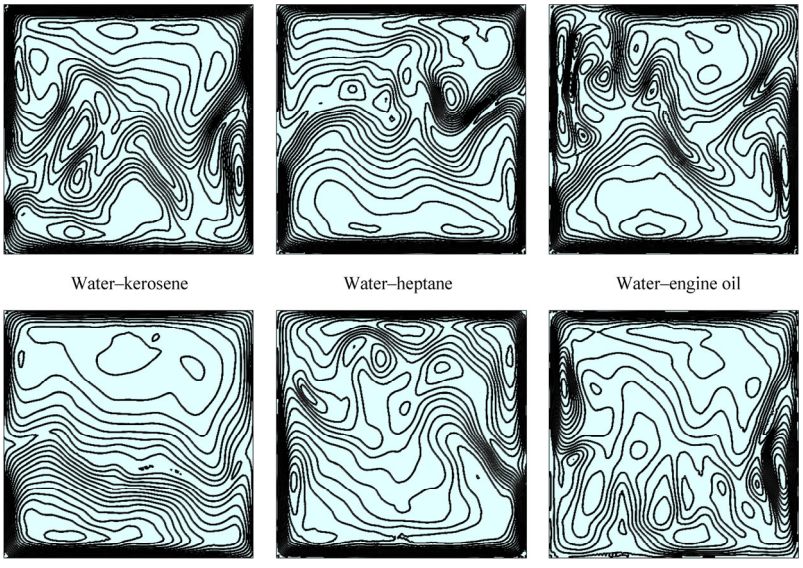

Fig. 9(a) Comparison among different fluids for velocity contour with De = 180, ϕ = 0.0, t = 300 s, and L = 40 m at outer domain for aspect ratio 1:1.

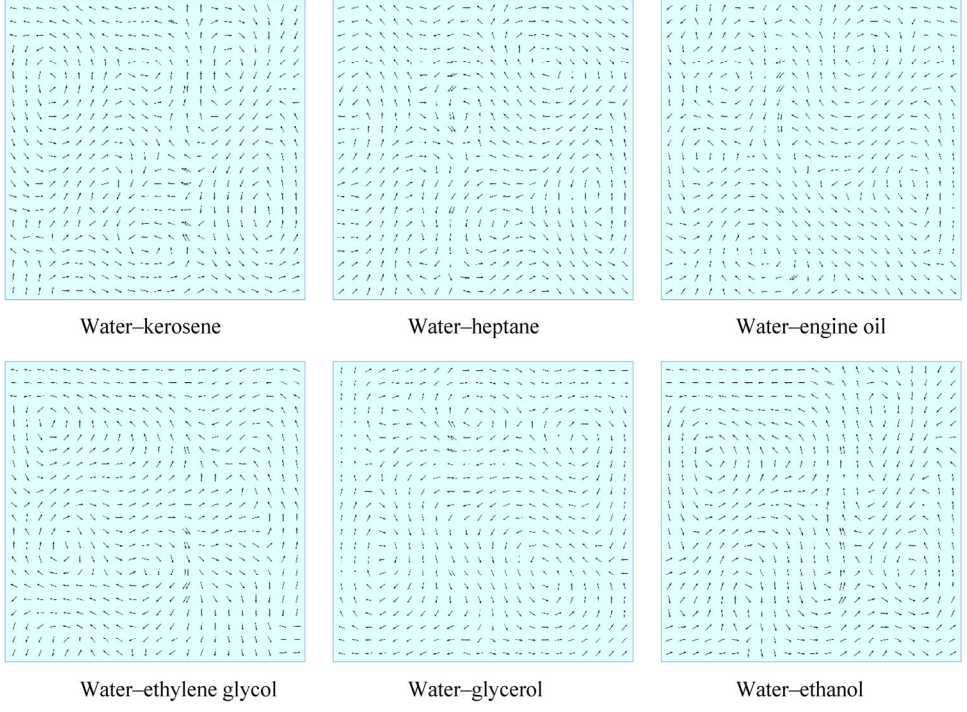

Fig. 9(b) Comparison among different fluids for vector plot of flow field with De = 180, ϕ = 0.0, t = 300 s, and L = 40 m at outer domain for aspect ratio 1:1.

form with just two orbits and a velocity of low-viscosity fluid that is greater than that of high-viscosity fluid.

The effect of aspect ratio on axial flow velocity is shown in Fig. 10(a), which shows that for aspect ratios 1:1, 1:2, 1:3, 1:4, 1:5, and 1:6 axial velocity are in hyperbolic shape having with multiple orbits. It is also observed that axial velocity for high-viscosity fluid is higher than low-viscosity fluid.

The aspect ratio influence on the velocity contour is shown in Fig. 10(b). There are ten contours and two domains of axial flow when the aspect ratio is 1:1. It demonstrates that there are four contours and that the axial flow is displaced close to the center of the duct channel for aspect ratios of 1:2, 1:3, and 1:4. Dean's flow is therefore similarly erratic. The axial flow is shifted closer to the center of the duct channel and the inner wall; however, when the aspect ratio is between 1:5 and 1:6, there are only two contours. Dean's flow is

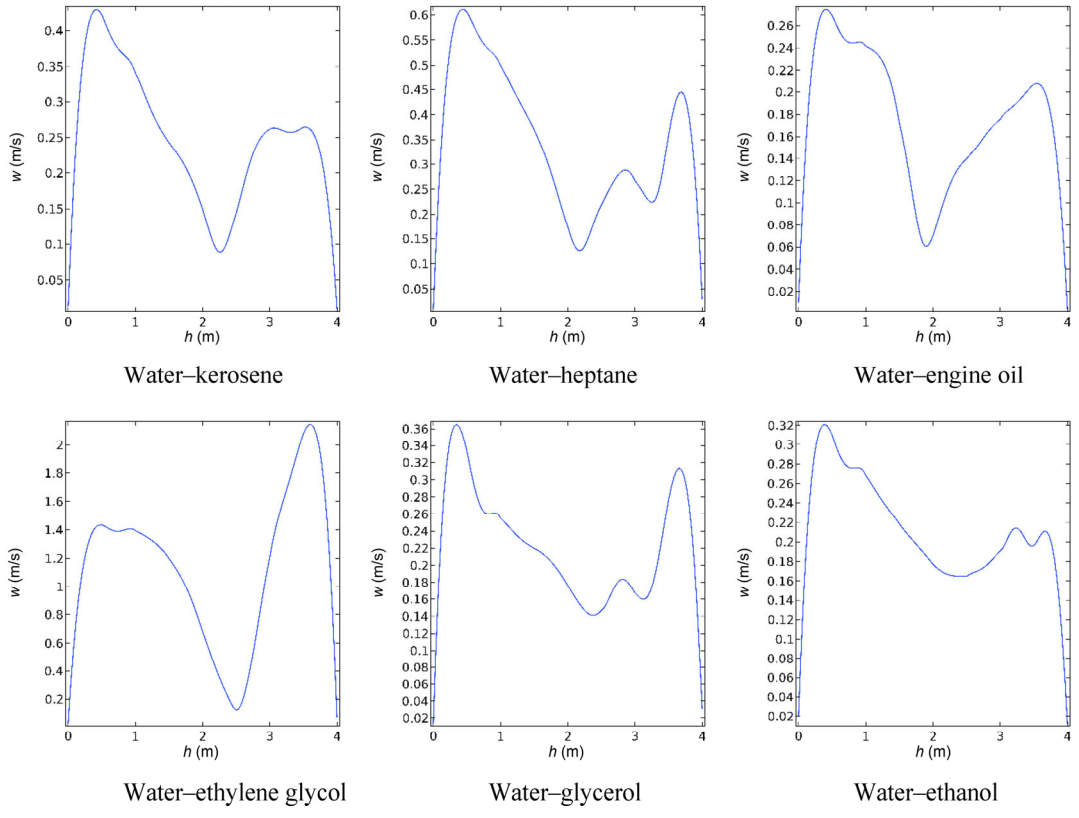

Fig. 9(c) Comparison among different fluids for axial flow velocity with $De = 180$, $\phi = 0.0$, $t = 300$ s, and $L = 40$ m at outer domain for aspect ratio 1:1.

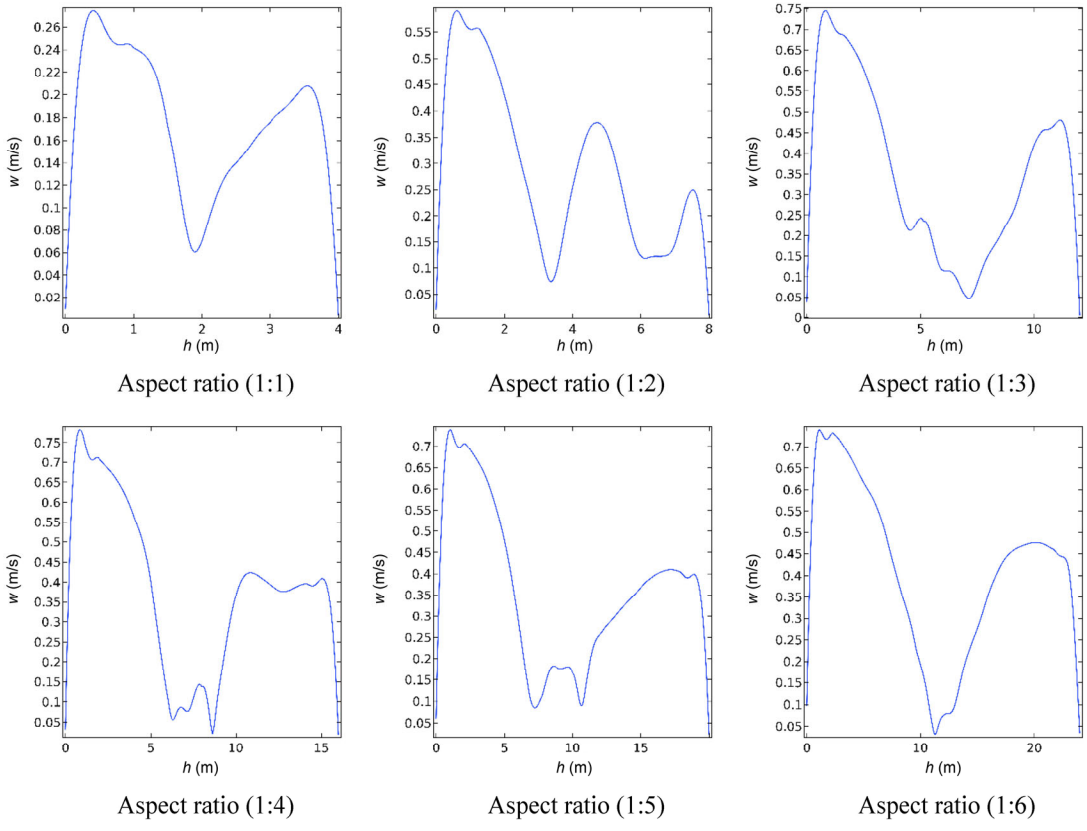

Fig. 10(a) Aspect ratio effect on axial flow velocity with $L = 40$ m, $De = 180$, $t = 300$ s, and $\phi = 0.0$ at outer domain.

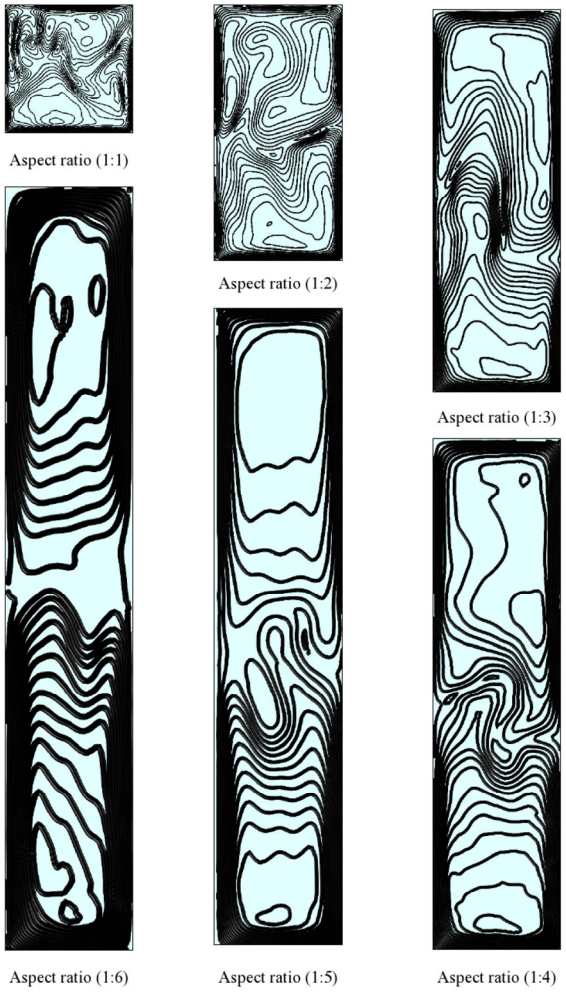

Fig. 10(b) Aspect ratio effect on velocity contour with L = 40 m, De = 180, t = 300 s, and ϕ = 0.0 at outer domain.

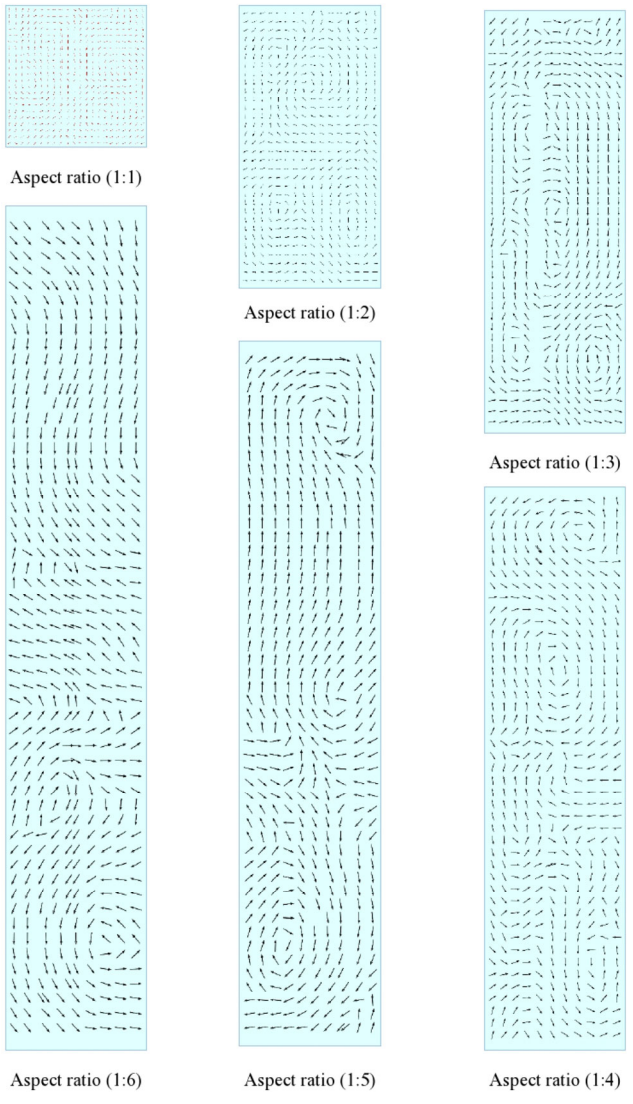

Fig. 10(c) Aspect ratio effect on vector plot of flow field with L = 40 m, De = 180, t = 300 s, and ϕ = 0.0 at outer domain.

therefore becoming consistent, i.e., steady state. Because fluid flow gets enough space to flow, the centrifugal force drives the fluid radially from the inner to the outer duct wall, setting up lateral fluid circulation.

The aspect ratio effect on the vector plot of the flow field is shown in Fig. 10(c). For secondary flow, there are six and four symmetric vortex solutions with aspect ratios of 1:1 and 1:2, respectively, and each pair of vortex is pointing in reverse directions. There are two symmetric vortex solutions and two asymmetric vortex solutions for secondary flow for aspect ratios 1:3 and 1:4. Asymmetric vortex pairs move in a direction normal to the boundary, while symmetric vortex pairs move in the opposite direction. The upper and lower walls of the secondary flow have two asymmetric vortices that are positioned there, and their trajectories are opposite when the aspect ratios are 1:5 and 1:6.

The average value of the magnitude of velocity at the surface on the cut plane is shown in Fig. 11. The effect of curvature radius is displayed in Fig. 11(a). It is observed that the velocity increases due to the increasing radius of curvature. For $L \geq 100$ m, the velocity behavior is like a straight duct. Figure 11(b) depicts the effect of the Dean number on the average value of surface velocity magnitude on the cut plane. When the Dean number increases, the velocity line also increases because the Dean number depends on the Reynolds number as well as inlet velocity. Figure 11(c) depicts the effect of particle concentration on the average value of surface velocity magnitude on the cut plane. The flow has a low velocity when particle concentration $\phi = 0.0$ and 1.0, and a higher velocity when particle concentration $\phi = 0.2$ and 0.8. But at $\phi = 0.4$, there is the highest velocity line.

Figure 11(d) illustrates how the average value of the surface cut-plane velocity magnitude increases as viscosity decreases. According to Fig. 11(e), increasing porosity causes velocity to increase. As seen in Fig. 11(f), velocity is better in a porous duct than a nonporous duct.

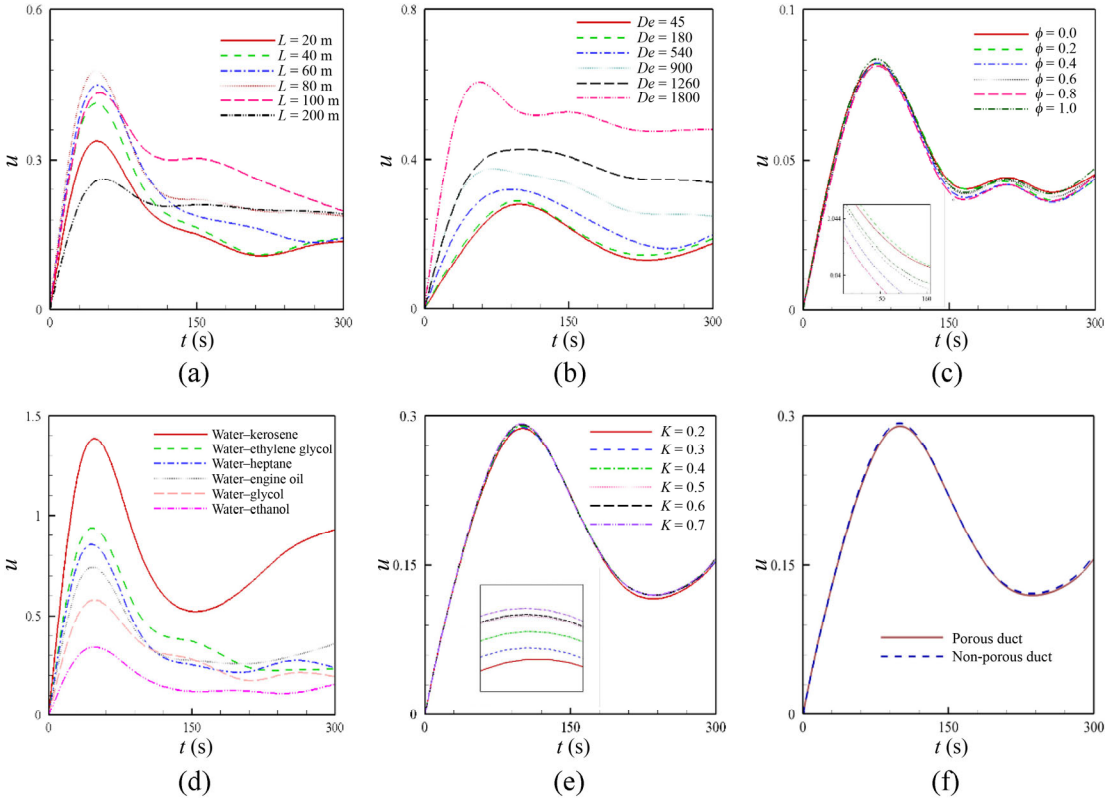

Fig. 11 Average value of the magnitude of the velocity at the surface of the cut plane for (a) effect of curvature, (b) effect of Dean number, (c) effect of particle concentration, (d) comparison of different fluid, (e) effect of porosity, and (f) comparison between porous and nonporous channels.

5 Conclusions

A 3D two-phase fluid flow in the porous medium through a curved duct with square and rectangular cross-sections was investigated numerically. The major findings are as follows:

- When increasing the radius of curvature, the number of contours reduces and Dean flow becomes chaotic to regular. If particle concentration increases on domain-1, i.e., decreases on domain-2, the Dean flow becomes chaotic to regular.
- Increasing the Dean number, the number of vortex decreases and Dean flow becomes periodic to balanced. Changing the aspect ratio from 1:1 to 1:6, number of vortex loses and the flow becomes periodic to steady.
- Comparison of two-phase flow between different fluids shows that the flow is steadier with high-viscosity fluid than with low-viscosity fluid. As time goes on, the volume fraction of mixed fluid becomes steady and high-density flow stays at the lower part and low-density flow stays on the upper part.
- When the radius curvature is low, the velocity line is high, and after increasing radius of curvature, the velocity reduces. For large radius of curvature, the velocity behaves like a straight channel. As the Dean number increases, so does the velocity line.
- Average value of velocity magnitude at the surface of the cut plane is low for particle concentration at $\phi = 0.0$, and 1.0, and it became high when $\phi = 0.5$. Average value of velocity magnitude increases due to increasing viscosity, and is better nonporous duct.

Acknowledgements

This work is done within the framework of the Ph.D. program of the first author under the Department of Mathematics, Bangladesh University of Engineering and Technology (BUET), Dhaka, Bangladesh. Financial support from the University Grant Commission (UGC), Bangladesh Fellowship program is acknowledged.

Declaration of competing interest

The authors have no competing interests to declare that are relevant to the content of this article.

References

Al Kalbani, K. S. 2016. Finite element analysis of unsteady natural convective heat transfer and fluid flow of nanofluids inside a tilted square enclosure in the presence of oriented magnetic field. *American Journal of Heat and Mass Transfer*, 3: 186–224.

Al-Jibory, M. W., Al-Turaihi, R. S., Al-Jibory, H. N. 2018. An experimental and numerical study for two-phase flow (water–air) in rectangular ducts with compound tabulators. *IOP Conference Series: Materials Science and Engineering*, 433: 012049.

Avramenko, A. A., Kobzar, S. G., Shevchuk, I. V., Kuznetsov, A. V., Basok, B. I. 2004. Laminar forced convection in curved channel with vortex structures. *Journal of Thermal Science*, 13: 143–150.

Bear, J. 1972. *Dynamics of Fluids in Porous Media*. New York: American Elsevier Publishing Company.

Biswas, A. K., Sinha, P. K., Mullick, A. N., Majumdar, B. 2012. Flow investigation in a constant area curved duct. *International Journal of Engineering Research and Applications*, 2: 1232–1236.

Chandra, A. K., Kishor, K., Mishra, P. K., Alam, M. S. 2016. Numerical investigations of two-phase flows through enhanced microchannels. *Chemical and Biochemical Engineering Quarterly*, 30: 149–159.

Chowdhury, R., Parvin, S., Khan, M. A. H. 2016. Natural convective heat and mass transfer in a porous triangular enclosure filled with nanofluid in presence of heat generation. *AIP Conference Proceedings*, 1754: 050004.

Crandall, D., Ahmadi, G., Smith, D. H. 2009. Comparison of experimental and numerical two-phase flows in a porous micro-model. *Journal of Computational Multiphase Flows*, 1: 325–340.

Datta, D., Gada, V. H., Sharma, A. 2011. Analytical and level-set method-based numerical study for two-phase stratified flow in a plane channel and a square duct. *Numerical Heat Transfer, Part A: Application*, 60: 347–380.

Dean, W. R. 1927. XVI. Note on the motion of fluid in a curved pipe. *The London, Edinburgh, and Dublin Philosophical Magazine and Journal of Science*, 4: 208–223.

Dean, W. R. 1928. LXXII. The stream-line motion of fluid in a curved pipe. *The London, Edinburgh, and Dublin Philosophical Magazine and Journal of Science*, 5: 673–695.

Devakar, M., Ramesh, K., Chouhan, S., Raje, A. 2017. Fully developed flow of non-Newtonian fluids in a straight uniform square duct through porous medium. *Journal of the Association of Arab Universities for Basic and Applied Sciences*, 23: 66–74.

Dong, Z. F., Ebadian, M. A. 1992. Effects of buoyancy on laminar flow in curved elliptic ducts. *Journal of Heat Transfer*, 114: 936–943.

Dwivedi, K., Khare, R. K., Paul, A. 2018. MHD flow through vertical channel with porous medium. *International Journal of Applied Engineering Research*, 13: 11923–11926.

Eustice, J. 1910. Flow of water in curved pipes. *Proceedings of the Royal Society of London Series*, 84: 107–118.

Eustice, J. 1911. Experiments on streamline motion in curved pipes. *Proceedings of the Royal Society of London Series*, 85: 119–131.

Garg, P., Picardo, J. R., Pushpavanam, S. 2014. Vertically stratified two-phase flow in a curved channel: Insights from a domain perturbation analysis. *Physics of Fluids*, 26: 073604.

Greenkorn, R. A. 1981. Steady flow through porous media. *AIChE Journal*, 27: 529–545.

Gyves, T. W. 1997. A numerical solution to conjugated mixed convection heat transfer in the curved square channel. Ph.D. Dissertation. New York, USA: The State University of New York at Stony Brook.

Gyves, T. W., Irvine, T. F., Naraghi, M. H. N. 1999. Gravitational and centrifugal buoyancy effects in curved square channels with conjugated boundary conditions. *International Journal of Heat and Mass Transfer*, 42: 2015–2029.

Hellström, G. 2007. Parallel computing of fluid flow through porous media. Ph.D. Dissertation. Luleå, Sweden: Luleå Tekniska Universitet.

Hoque, M. M., Alam, M. M. 2013. Effects of Dean number and curvature on fluid flow through a curved pipe with magnetic field. *Procedia Engeering*, 56: 245–253.

Keshtekar, M. M., Asadi, M. H., Samareh, R., Poor, H. M. 2014. Numerical study on the effects of Marangoni-driven boundary layer flow for different nanoparticles with variable based fluids. *Journal of International Academic Research for Multidisciplinary*, 2: 806–815.

Khan, M. A. H. 2006. Singularity behavior of flow in a curved pipe. *Journal of Applied Mechanics & Engineering*, 11: 699–704.

Khan, M. A. H., Hye, M. A. 2007. Dominating singularity behavior of flow in a nonaligned straight rotating pipe. *International Journal of Fluid Dynamics Research*, 34: 562–571.

Khuri, S. A. 2006. Stokes flow in curved channels. *Journal of Computational and Applied Mathematics*, 187: 171–191.

Kucuk, H. 2010. Numerical analysis of entropy generation in concentric curved annular ducts. *Journal of Mechanical Science and Technology*, 24: 1927–1937.

Mondal, R. N., Alam, M. M., Yanase, S. 2007. Numerical prediction of non-isothermal flows through a rotating curved duct with square cross section. *Science & Technology Asia*, 12: 24–43.

Nadeem, S., Shahzadi, I. 2015. Mathematical analysis for peristaltic flow of two phase nanofluid in a curved channel. *Communication of Theoretical Physics*, 64: 547–554.

Norouzi, M., Biglari, N. 2013. An analytical solution for Dean flow in curved ducts with rectangular cross section. *Physics of Fluids*, 25: 053602.

Okechi, N. F., Asghar, S. 2019. Fluid motion in a corrugated curved channel. *The European Physical Journal Plus*, 134: 165.

Okechi, N. F., Asghar, S. 2021. Two-phase flow in a groovy curved channel. *European Journal of Mechanics - B/Fluids*, 88: 191–198.

Olsson, E., Kreiss, G. 2005. A conservative level set method for two phase flow. *Journal of Computational Physics*, 210: 225–246.

Olsson, E., Kreiss, G. Zahedi, S. 2007. A conservative level set method for two phase flow II. *Journal of Computational Physics*, 225: 785–807.

Osher, S., Sethian, J. A. 1988. Fronts propagating with curvature-dependent speed: Algorithms based on Hamilton–Jacobi formulations. *Journal of Computational Physics*, 79: 12–49.

Picardo, J. R., Garg, P., Pushpavanam, S. 2015. Centrifugal instability of stratified two-phase flow in a curved channel. *Physics of Fluids*, 27: 054106.

Roy, S., Sinha, S., Hansen, A. 2020. Flow-area relations in immiscible two-phase flow in porous media. *Frontiers in Physics*, 8: 4.

Sharma, A. 2015. Level set method for computational multi-fluid dynamics: A review on developments, applications and analysis. *Sadhana*, 40: 627–652.

Sussman, M., Smereka, P., Osher, S. 1994. A level set approach for computing solutions to incompressible two-phase flow. *Journal of Computational Physics*, 114: 146–159.

Thangam, S., Hur, N. 1990. Laminar secondary flows in curved rectangular ducts. *Journal of Fluid Mechanics*, 217: 421–440.

Xu, J. L., Cheng, P., Zhao, T. S. 1999. Gas–liquid two-phase flow regimes in rectangular channels with mini/micro gaps. *International Journal of Multiphase Flow*, 25: 411–432.